*metals*

MDPI

*Article*

# Speciation of Manganese in a Synthetic Recycling Slag Relevant for Lithium Recycling from Lithium-Ion Batteries

**Alena Wittkowski [1], Thomas Schirmer [2], Hao Qiu [3], Daniel Goldmann [3] and Ursula E. A. Fittschen [1,*]**

[1] Institute of Inorganic and Analytical Chemistry, Clausthal University of Technology, Arnold-Sommerfeld Str. 4, 38678 Clausthal-Zellerfeld, Germany; alena.wittkowski@tu-clausthal.de
[2] Department of Mineralogy, Geochemistry, Salt Deposits, Institute of Disposal Research, Clausthal University of Technology, Adolph-Roemer-Str. 2A, 38678 Clausthal-Zellerfeld, Germany; thomas.schirmer@tu-clausthal.de
[3] Department of Mineral and Waste Processing, Institute of Mineral and Waste Processing, Waste Disposal and Geomechanics, Clausthal University of Technology, Walther-Nernst-Str. 9, 38678 Clausthal-Zellerfeld, Germany; hao.qiu@tu-clausthal.de (H.Q.); daniel.goldmann@tu-clausthal.de (D.G.)
* Correspondence: ursula.fittschen@tu-clausthal.de; Tel.: +49-5323-722205

**Abstract:** Lithium aluminum oxide has previously been identified to be a suitable compound to recover lithium (Li) from Li-ion battery recycling slags. Its formation is hampered in the presence of high concentrations of manganese (9 wt.% $MnO_2$). In this study, mock-up slags of the system $Li_2O$-CaO-$SiO_2$-$Al_2O_3$-MgO-$MnO_x$ with up to 17 mol% $MnO_2$-content were prepared. The manganese (Mn)-bearing phases were characterized with inductively coupled plasma optical emission spectrometry (ICP-OES), X-ray diffraction (XRD), electron probe microanalysis (EPMA), and X-ray absorption near edge structure analysis (XANES). The XRD results confirm the decrease of $LiAlO_2$ phases from Mn-poor slags (7 mol% $MnO_2$) to Mn-rich slags (17 mol% $MnO_2$). The Mn-rich grains are predominantly present as idiomorphic and relatively large (>50 µm) crystals. XRD, EPMA and XANES suggest that manganese is present in the form of a spinel solid solution. The absence of light elements besides Li and O allowed to estimate the Li content in the Mn-rich grain, and to determine a generic stoichiometry of the spinel solid solution, i.e., $(Li_{(2x)}Mn^{2+}{}_{(1-x)})_{1+x}(Al_{(2-z)},Mn^{3+}{}_z)O_4$. The coefficients $x$ and $z$ were determined at several locations of the grain. It is shown that the aluminum concentration decreases, while the manganese concentration increases from the start ($x$: 0.27; $z$: 0.54) to the end ($x$: 0.34; $z$: 1.55) of the crystallization.

**Keywords:** lithium; engineered artificial minerals (EnAM); X-ray absorption near edge structure (XANES); powder X-ray diffraction (PXRD); electron probe microanalysis (EPMA); melt experiments



**Citation:** Wittkowski, A.; Schirmer, T.; Qiu, H.; Goldmann, D.; Fittschen, U.E.A. Speciation of Manganese in a Synthetic Recycling Slag Relevant for Lithium Recycling from Lithium-Ion Batteries. *Metals* **2021**, *11*, 188. https://doi.org/10.3390/met11020188

Academic Editor: Mark E. Schlesinger
Received: 30 December 2020
Accepted: 18 January 2021
Published: 21 January 2021



## 1. Introduction

Modern technologies, such as renewable energy and e-mobility, demand a new portfolio of technology-critical elements and materials. Limited resources, national policies or monopolies threaten the supply of some technology-critical elements. Hence, the recovery of these elements from waste is crucial. On the one hand, demand for lithium (Li) has increased rapidly due to the popularity and extraordinary performance of Li-ion batteries. On the other hand, Li is produced by mainly two countries, Australia (ca. 55%) and Chile (ca. 23%) [1]. The recycling of some components from Li-ion batteries is already put into practice, e.g., cobalt, in a pyrometallurgical process [2,3]. Pyrometallurgical recycling has the benefit of being adaptable to many waste streams; additionally, the emission of toxic compounds like HF is prevented. Due to its ignoble character, Li is driven into the slag and is usually not recovered.The recovery of Li from pyrometallurgical recycling slags can be accomplished by the targeted formation of "engineered artificial minerals" (EnAM).

The strategy of EnAM formation is to concentrate the elements of interest in a few phases, with a structure and size that allows an efficient separation. Figure 1 shows a

scheme of EnAM formation. The target element (yellow triangle) spreads over several different phases (red and green forms) and the matrix (blue) in the unmodified slag (top picture). The target element will be difficult to isolate due to its occurrence in many different phases. The goal in EnAM is to concentrate the target element in a single phase (red pentagon, bottom picture) that differs physically and chemically from the other phases (green hexagon), and allows for efficient separation and further treatment.

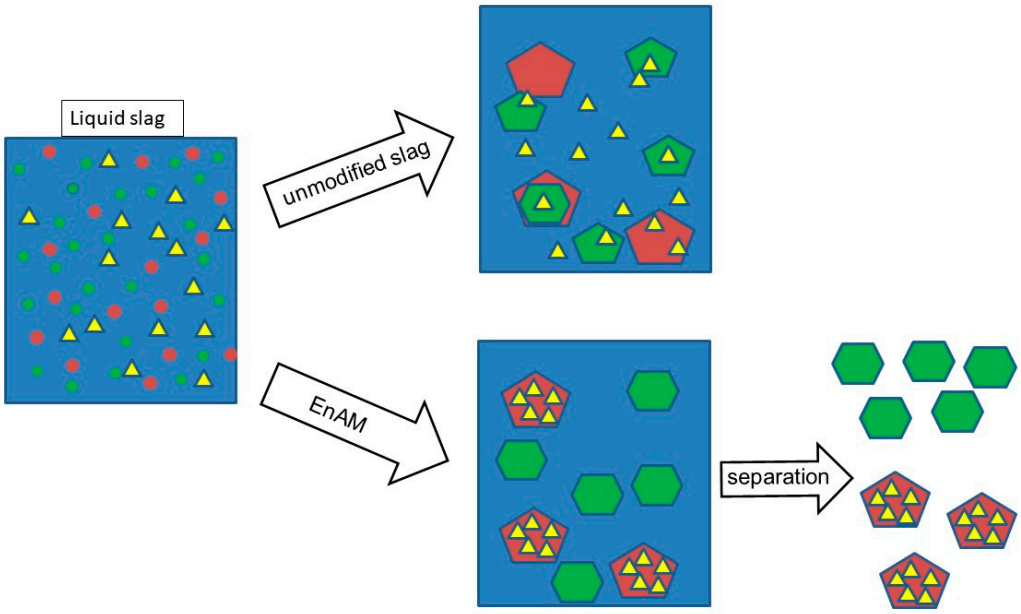


**Figure 1.** Sketch of engineered artificial minerals (EnAM) formation. On the left, different elements are shown in the liquid slag-matrix: target element (yellow triangle), phase for EnAM (red) and other phases (green). The upper route refers to an unmodified slag–the target element is spread over several different phases and the matrix (blue). The target element is not recovered. The bottom picture illustrates the formation of EnAM. The target element is concentrated in a single phase (red pentagon) that differs physically and chemically from the other phases (green hexagon), and allows for efficient separation and further treatment.

Separation of artificial minerals, enriched in valuable elements from remaining slag components, might be carried out by flotation processes. Here, the composition and structure of phases are crucial. It can be expected that none of the artificially produced minerals will show hydrophobic behavior by nature. Thus, the mineral-collector-interaction has to be studied, and this interaction relies strongly on crystal structure and ions, responsible for the adsorption of the active group of collector molecules.

The recovery of Li from slags has been subject to several studies. Elwert et al. [2] found that Li reacts with aluminum to form predominately large lithium aluminate ($LiAlO_2$) crystals. The aluminum binds Li from the melt uniformly in one phase at an early state of solidifying phase of the molten slag. The idiomorphic to hypidiomorphic lithium aluminate crystals can easily be separated from the matrix by flotation. Hence, lithium aluminate is a promising EnAM candidate. The recovery of Li from $LiAlO_2$ was successfully conducted by Haas et al. [4]. Elwert et al. [5] investigated a hydrometallurgical process to recover Li from slags with low aluminum compared to [2] and enriched in silicone. However, it was found that the formation of $LiAlO_2$ is suppressed in manganese (Mn)-rich slags [2]. In these slags, Li is distributed over several phases of low crystallinity. Elements like Mn seem to have a significant influence on the formation of compounds and grain size during the formation of the slag. Due to the increasing amount of Li-ion batteries with Mn-based cathode materials, i.e., Li-$Ni_xMn_yCo_zO_2$ (NMC), it must be assumed that the Mn content in battery waste streams will increase soon. Accordingly, it is necessary to understand the role of the redox-active Mn on the genesis of crystalline, and especially amorphous grains

from the ionic melts. A careful characterization of the Mn-bearing grains will give insight into these processes. The first survey with mineralogical and thermodynamic methods on the formation of Li-EnAMs was conducted by Schirmer et al. [6] on a similar system, but without Mn. Their study shows that formation of spinel solid solutions is a favorable reaction with a thermodynamically proved potential to scavange Li from the slag in an early stage of the solidification. Adding Mn to this system would result in more complex solidification reactions with Mn-containing spinel solid solutions in particular, as numerous spinel-like oxides of Li and Mn are already described [7].

Therefore, in this study, Li- and Mn-bearing phases from a synthetic slag, in the following termed mock-up slag (MUS), of the system $Li_2O$-CaO-$SiO_2$-$Al_2O_3$-MgO-$MnO_x$, with up to 17 mol% $MnO_2$-content, are studied. The crystalline components are determined by powder X-ray diffraction (PXRD). The main Mn-containing phase could be identified as an oxide solid solution of spinel-type using electron probe microanalysis (EPMA). From a combination of the virtual compounds $LiMnO_2$, $Mn_{0.5}AlO_2$ (1/2 galaxite spinel) and $Mn_{0.5}MnO_2$ (1/2 hausmannite), the formula $(Li_{(2x)}Mn^{2+}{}_{(1-x)})_{1+x}(Al_{(2-z)},Mn^{3+}{}_z)O_4$ was calculated. This matches with the PXRD results, as all main reflections of the oxides are located between those of $LiAl_5O_8$ and $MnAl_2O_4$. The EPMA and PXRD analysis showed that a high amount of grains are amorphous or of low crystallinity. The PXRD falls short of giving insight into the Mn species in amorphous phases. EPMA allows recognizing individual crystalline and amorphous phases. For amorphous phases, however, stoichiometric information can usually not be extracted from the data. Hence, laboratory-based X-ray absorption near edge structure (XANES) is applied here to determine the bulk Mn species of the crystalline and the amorphous components of the slag. The findings from this independent method confirmed the Mn oxidation state as being between +2 and +3, as well as the presence of Mn spinel structures.

## 2. Background

The following section gives a short introduction to the relevant binary subsystems of the $Al_2O_3$-$MnO_x$-$Li_2O$ ternary system, which itself is not yet published. This will allow putting the presented results into the mineralogical context. In addition, the methods used to investigate the oxidation state of Mn are briefly described.

### *2.1. The System $Li_2O$-$MnO_x$ with Focus on Spinel Structures*

The stoichiometric spinel $LiMn_2O_4$ and several other spinel phases of Li-Mn-O are known in the $Li_2O$-$MnO_x$ system. Paulsen and Dahn [7] created a binary phase diagram of Li-Mn-O in air. They described a spinel with the formula $Li_{(1+x)}Mn_{(2-x)}O_4$ to be stable between 400 and 880 °C. With the rising temperature, $x$ decreases from 1/3 at 400 °C to 0 at 880 °C. Below 400 °C, the only stable spinel phases are $Li_4Mn_5O_{12}$ and $LiMn_{1.75}O_4$. Raising the temperature above 880 °C leads to the replacement of Li by Mn and tetragonal spinel $[Li_{(1-x)}Mn_x]MnO_4$ [7].

### *2.2. The System $Li_2O$-$Al_2O_3$*

The binary system $Li_2O$-$Al_2O_3$ exhibits several phases. Konar et al. [8] described $LiAl_5O_8$ spinel, $LiAl_{11}O_{17}$, $LiAlO_2$ and $Li_5AlO_4$.

$LiAl_5O_8$ is described as an inverse spinel structure with $Al^{3+}$ on tetrahedral sites and $Li^+$ and the remaining $Al^{3+}$ on octahedral sites. A polymorphic transition to this spinel structure occurs from the stoichiometric phase. $LiAl_{11}O_{17}$ is a high-temperature phase, only stable above 1537 °C. For $LiAlO_2$, a polymorphic transition from $\alpha$- to $\gamma$-phase occurs.

$Li_5AlO_4$ crystallizes below 50 mol% $Al_2O_3$, in a mixture either with $LiAlO_2$ or with $LiO_2$ [8].

### *2.3. The System $Al_2O_3$-$MnO_x$*

Solid solutions of spinel oxide type ($XY_2O_4$) with a cubic and tetragonal crystal system are described by Chatterjee et al. [9] to form in the $Al_2O_3$-MnO-$Mn_2O_3$ system. Besides

the cubic $MnAl_2O_4$ (galaxite), additionally, $MnMn_2O_4$ (hausmannite) with a tetragonal and cubic crystal system (transformation tetragonal -> cubic: 1172 °C in the air) can occur. While the tetragonal form of hausmannite incorporates only a small amount of galaxite, the cubic variety forms a solid solution.

### *2.4. Speciation of Oxidation States in Spinel Systems*

Recycling slags are usually complex elemental mixtures comprising various components and phases. Due to uncontrolled and–in geological terms–fast cooling conditions, only a few components in these slags are crystalline. Crystalline phases are easily accessible by established methods like PXRD.

The amorphous components, however, elude the identification by PXRD. Wet chemical methods like inductively coupled plasma atomic emission spectroscopy (ICP-OES) yield information on the stoichiometric composition, but fall short for the speciation. EPMA allows studying crystalline and amorphous phases. Stoichiometric information can be obtained for crystalline phases with reasonable certainty. Structure predictions on non-crystalline phases, however, are merely estimations. XANES is a convenient method to analyze the species of 3d-elements in crystalline, as well as amorphous materials. Asaoka et al. determined the oxidation state of Mn in granulated coal ash via XANES [10], while Kim et al. used XANES for Mn speciation in steel-making slags [11]. In general, the oxidation state, the coordination sphere, and in some cases the actual compound can be determined. Usually, this method is exclusively available at synchrotron sources (Sy). Here, a laboratory-based XANES spectrometer was used, which allows everyday access to measure several routine samples or improve sample preparation. The set-up is described by Seidler et al. [12,13]. Laboratory-based XANES has been used successfully in catalysis research, as well as for the determination of vanadium oxidation state in catalysts and vanadium redox flow batteries [14–16].

## 3. Materials and Methods

### *3.1. Synthesis of the Mock-Up Slag*

The chemicals used for producing the mock-up slags are lithium carbonate (Merck KGaA purum, Darmstadt, Germany), calcium carbonate (Sigma-Aldrich, reagent grade, St. Louis, MO, USA), silicon dioxide (Sigma-Aldrich, purum p.a., St. Louis, MO, USA), aluminum oxide (Merck KGaA, Darmstadt, Germany), magnesium oxide (98%, Roth, Karlsruhe, Germany) and manganese dioxide (Merck KGaA, reagent grade, Darmstadt, Germany).

The concentrations of the reactants of the slag synthesis are the following: For V-1 32 mol% $Al_2O_3$ were mixed with 16 mol% CaO, 21 mol% $Li_2O$, 3 mol% MgO, 7.4 mol% $MnO_2$, and 22 mol% $SiO_2$. For V-2, 29 mol% $Al_2O_3$ were mixed with 14 mol% CaO, 19 mol% $Li_2O$, 3 mol% MgO, 13 mol% $MnO_2$, and 21 mol% $SiO_2$. For V-3, 28 mol% $Al_2O_3$ were mixed with 14 mol% CaO, 18 mol% $Li_2O$, 3 mol% MgO, 17 mol% $MnO_2$, and 20 mol% $SiO_2$. The chemicals were manually mixed in a mortar and ground in a disc mill for 5 min. Each sample was placed in a Pt-Rh crucible and heated in a chamber furnace (Nabertherm HT16/17, Nabertherm GmbH, Lilienthal, Germany) in an ambient air atmosphere. The temperature program is shown in Figure 2. A heating rate of 2.89 °C/min was initially employed to reach 720 °C, which is the melting temperature of $Li_2CO_3$. Subsequently, a heating rate of 1.54 °C/min was used to decompose $Li_2CO_3$ and reach the target temperature of 1600 °C. Finally, the obtained MUS were kept at 1600 °C for two hours. After that, the samples were cooled to 500 °C at a cooling rate of 0.38 °C/min, and quenched in water. Three MUS V-1-3 were obtained. For PXRD and XANES measurements, parts of the obtained slag were ground for five minutes in a disc mill (Siebtechnik GmbH, Mühlheim an der Ruhr, Germany).

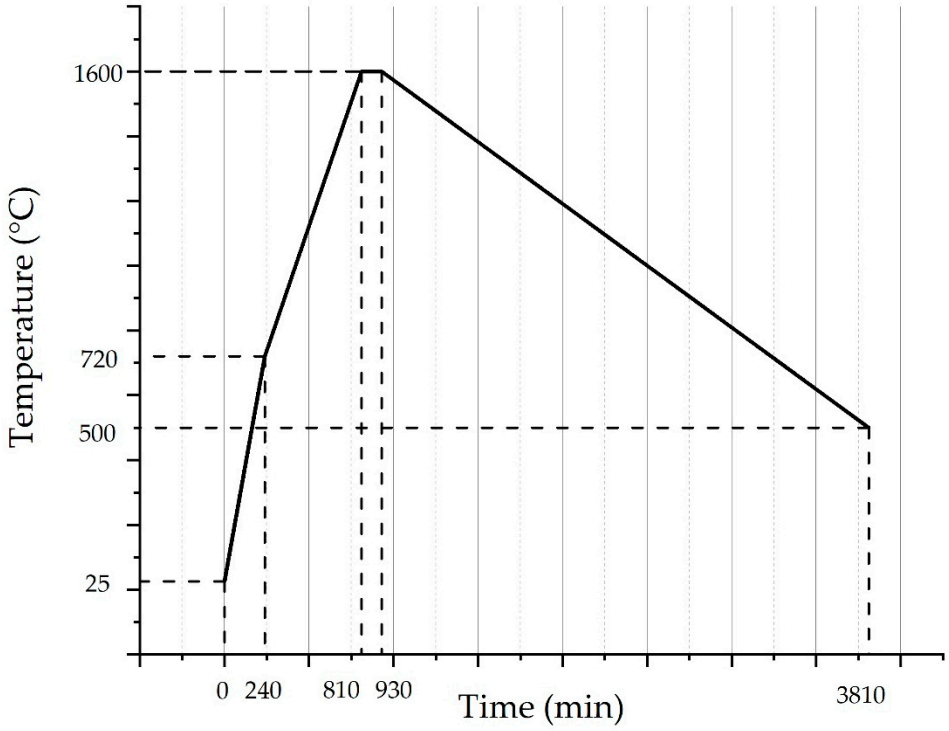


**Figure 2.** Temperature program of the chamber furnace. A heating rate of 2.89 °C/min was employed to reach the melting temperature of $Li_2CO_3$ at 720 °C, followed by a heating rate of 1.54 °C to the target temperature of 1600 °C. The temperature was held for 120 min, and afterward, a cooling rate of 0.38 °C/min was employed to reach a temperature of 500 °C.

The elemental content was determined by ICP-OES (ICP-OES 5100, Agilent, Agilent Technologies Germany GmbH & Co. KG, Waldbronn, Germany). The samples were fused with sodium tetraborate in a platinum crucible at 1050 °C, and then leached with diluted hydrochloric acid to determine Al, Ca, Li, Mg, Ti and Si. To determine other elements, the samples were suspended in nitric acid and digested at 250 °C and under a pressure of 80 bar in an autoclave (TurboWAVE, MLS, Leutkirch im Allgäu, Germany).

### *3.2. Synthesis of Galaxite via Solution Combustion Synthesis*

Artificial galaxite was prepared via solution combustion synthesis. Aluminum nitrate nonahydrate (VWR chemicals, Darmstadt, Germany, analytical reagent, min. 98%) and manganese (II) nitrate tetrahydrate (Merck, KGaA, Darmstadt, Germany, pro analysi, min 98.5%) were used as oxidizers and mixed in stoichiometric ratio 1:2. Aluminum nitrate nonahydrate (7.5 g) was mixed with manganese (II) nitrate tetrahydrate (2.5 g). As a fuel, urea (Merck KGaA, Darmstadt, Germany, pro analysi, min. 99.5%) was added in excess (5 g). All components were dissolved in water. The solution was heated with a Bunsen burner until near dryness. The mixture was ignited with a second Bunsen burner. Purity was verified by PXRD (STOE STADI P, STOE & Cie GmbH, Hilpertstraße 10, 64295 Darmstadt, Germany).

### *3.3. Powder X-ray Diffraction*

The analysis of the bulk mineralogical composition was provided by PXRD, using a PANalytical X-Pert Pro diffractometer, equipped with a Co-X-ray tube (Malvern Panalytical GmbH, Nürnberger Str. 113, 34123 Kassel, Germany). For identification of the compounds, the PDF-2 ICDD XRD database [17], the American Mineralogist Crystal Structure Database [18] and the RRUFF-Structure database [19] were evaluated.

### *3.4. Electron Probe Microanalysis*

The analysis of single crystals and grains was performed with EPMA. EPMA is a standard method to characterize the chemical composition in terms of single spot analysis or element distribution patterns, accompanied by electron backscattered Z (ordinal number) contrast (BSE(Z)) or secondary electron (SE) micrographs. The EPMA measurements were performed on samples, which were embedded in epoxy resin, polished and coated with carbon. They were characterized using a Cameca $SX^{FIVE}$ FE (Field Emission) electron probe, equipped with five wavelength dispersive (WDX) spectrometers (CAMECA SAS, 29, quai des Grésillons, 92230 Gennevielliers, Cedex, France). To calibrate the wavelength dispersive X-ray fluorescence spectrometers (WDXRF), an appropriate suite of standards and analyzing crystals was used. The reference materials were provided by P&H Developments (The Shire 85A Simmondley village, Glossop, Derbyshire SK13 9LS, UK and Astimex Standards Ltd., 72 Milicent St, Toronto, ON, M6H 1W4, Canada). The beam size was set to zero, leading to a beam diameter of substantially below 1 µm (100–600 nm with field emitters of Schottky-type, e.g., [20]). To evaluate the measured intensities, the X-PHI-Model was applied [21].

Li, one of the key elements in this study, cannot be directly analyzed, since EPMA uses X-ray emission to detect the elements in the sample, and the extremely low fluorescence yield and long wavelength of the Li K$\alpha$ render the direct determination of this element merely impossible. With the reasonable assumption that other refractory light elements like Be and B are not present in the investigated material and volatile elements and compounds like F, $H_2O$, $CO_2$ or $NO_3^-$ are effectively eliminated during the melt experiment, Li can be calculated using virtual compounds. Where necessary, the balanced Li concentration was included in the matrix correction calculation. To access the analytical accuracy with respect to the determination of Li, the international reference material spodumene (Astimex Standards Ltd., Toronto, ON, Canada) and the in-house standard $LiAlO_2$ were analyzed (Table 1).

**Table 1.** Recovery of Li-compounds. Spod: spodumene, % StdDev: Relative standard deviation in percent, Repeats: N = 5, R: Recovery, LiAl: $LiAlO_2$.

| Wt.% | Average Spod. | %StDev., Spod. | Ref. Spod. | R (%) | Average LiAl | %StDev., LiAl | Ref. LiAl | R (%) |
|---|---|---|---|---|---|---|---|---|
| **Al** | 15.04 | 0.35 | 14.4 | 104 | 41.24 | 0.22 | 40.9 | 101 |
| **Mg** | 0.00 | n.a. | 0.0 | n.a. | 0.01 | n.a. | 0.0 | n.a. |
| **Ti** | 0.00 | n.a. | 0.0 | n.a. | 0.00 | n.a. | 0.0 | n.a. |
| **Mn** | 0.05 | n.a. | 0.0 | n.a. | 0.00 | n.a. | 0.0 | n.a. |
| **Fe** | 0.02 | n.a. | 0.0 | n.a. | 0.03 | n.a. | 0.0 | n.a. |
| **Ca** | 0.01 | n.a. | 0.0 | n.a. | 0.01 | n.a. | 0.0 | n.a. |
| **K** | 0.00 | n.a. | 0.0 | n.a. | 0.00 | n.a. | 0.0 | n.a. |
| **Si** | 28.71 | 0.56 | 30.0 | 96 | 0.01 | n.a. | 0.0 | n.a. |
| **Na** | 0.10 | 2.83 | 0.09 | 112 | 0.00 | n.a. | 0.0 | n.a. |

### *3.5. X-ray Absorption near Edge Structure*

The Mn speciation was achieved with XANES. Other than usual, XANES was not conducted at a synchrotron facility but using a laboratory-based device, the easyXES100-extended (short: easyXES100; easyXAFS LLC, Renton, WA, USA). To enable these measurements with high energy resolution comparable to that obtained at synchrotron facilities, a Rowland circle Johann-type monochromator is used, see Figure 3. The instrument comprises an X-ray tube (100 W, air-cooled tube with W/Pd anode, 35 kV maximum accelerating potential), a spherically bent crystal analyzer (SBCA, Si 110) and an SDD detector (AXAS-M1, KETEK, Munich, Germany). The components are positioned on scissor drives.

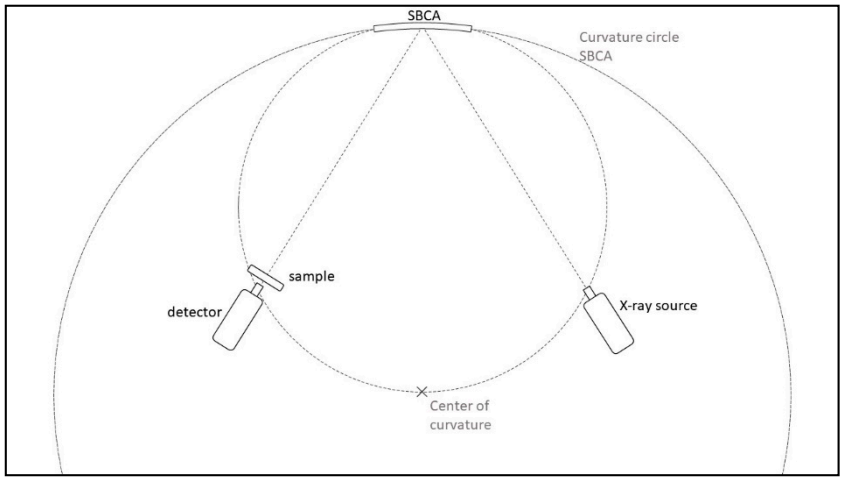


**Figure 3.** Scheme of the Rowland circle monochromator. The outer circle represents the curvature of the SBCA. The inner circle has a diameter matching the radius of the curvature circle. On this inner circle, the X-ray source and the detector are positioned. The sample is positioned right in front of the detector. The components are set on a scissor drive, allowing fine energy scanning.

This enables energy scanning by synchronously and symmetrically moving the detector and the source. The SBCA sits on a passively driven slider in the Rowland circle, which is coupled to the X-ray source stage. This way, the proper positioning of all three components is elegantly achieved. A helium-filled box is installed in the beam path, to lower background absorption and scattering by air. This set-up allows energy scanning with a resolution of about 1 eV. Further information about the set-up is published by Seidler et al. and Jahrman et al. [12,13,22]. At every energy step, an energy-dispersive X-ray spectrum (EDX) is acquired. The area of interest is automatically integrated by the software based on labVIEW2017 [23]. This way, a file with the relevant information on the energy and counts per lifetime is created and used together with the $I_0$ measurement to obtain the XANES.

Spectra of manganese dioxide (Merck AG, Darmstadt, Germany, for synthesis) were recorded, validated with spectra from the literature, i.e., spectra from Hokkaido University, Japan [24,25] and subsequently used as reference for energy calibration. The scans in the $\theta$-angle space are converted to the energy space (see Appendix A).

The XANES of references and samples were recorded and processed as follows: The Mn K-edge was scanned from 6482 eV to 6800 eV (SBCA, Si 110, $n = 4$; see Appendix A), with a step width of 0.25 eV. At each step, an EDX spectrum with a 10 s live time was obtained, resulting in a total measurement time of *approx.* 3.5 h per spectrum. Three samples of MUS V-3 were prepared in parallel by mixing the finely ground slag with Vaseline (ISANA; Dirk Rossmann GmbH, Burgwedel, Germany) in a weight ratio of 2/3 Vaseline and 1/3 MUS powder. The mixtures were placed in washers with a height of 0.1 mm to adjust the thickness of the samples. The washer was sealed from both sides with adhesive tape (tesapack, tesa SE, Norderstedt, Germany) to hold the sample inside, and protect it from environmental influences. Each replicate was analyzed three times. The following Mn species were used as references: manganese (II) oxide (*oxidation state of manganese: +2*; alfa aesar, Thermo fisher (Kandel) GmbH, Kandel, Germany, 99%); synthetic galaxite ($Mn^{2+}Al_2{}^{3+}O_4$; *oxidation state of manganese: +2*), manganese (II, III) oxide (*average oxidation state of manganese: +2.67*; Sigma-Aldrich Chemie GmbH, Steinheim, Germany, 97%); braunite ($Mn^{2+}Mn^{3+}{}_6[O_8 \mid SiO_4]$; *formal oxidation state of manganese: +2.85*; Friedrichroda, Thuringia, Germany; obtained from Geo collection, Clausthal University of Technology); bixbyite ($Mn_2O_3$; *oxidation state of manganese: +3*; Paling Mine, Republic of South Africa; obtained from Geo collection, Clausthal university of technology); and

manganese (IV) oxide (*oxidation state of manganese: +4*; Merck AG, Darmstadt, Germany, for synthesis). They were prepared in the same way as the actual sample.

An additional $I_0$ spectrum of an empty washer sealed with adhesive tape was separately acquired for every measurement to calculate the absorption coefficient $\mu$(E) according to the equation: $\mu(\mathrm{E}) = -\ln I \cdot I_0^{-1}$. The average post-edge absorption $\mu$(E) (post edge line) in each spectrum was normalized to unity using ATHENA software [26]. Spectra from the same Mn species were merged in ATHENA and used for further analysis.

## 4. Results

The results of the characterization of the MUS V-1-3, which are supposed to match Li-ion battery recycling slags, are presented in this section. The composition was chosen to be similar to recycling slags characterized previously by Elwert et al. [2]. The methodology applied to study the MUS chemistry comprises ICP-OES, PXRD, EPMA and XANES.

Initially, the composition of the reactants and the products was determined by ICP-OES. The suppression of the formation of $LiAlO_2$ EnAM in MUS with increasing Mn content was studied by PXRD. The microstructure and microscopic elemental composition of the MUS with the highest Mn-content (MUS V-3; $MnO_2$: 17 mol%) were studied by BSE(Z) micrographs, as well as detailed spatially resolved quantitative point measurements and element distribution profiles, recorded with EPMA. From these results, a hypothesis for the genesis of the Mn-rich grains was established. This hypothesis is discussed in detail in Section 4.3. Finally, it was evaluated by studying the Mn species using XANES.

### *4.1. Bulk Chemistry*

The elemental composition of the reactants and the product slags were determined by digestion, followed by ICP-OES. The Mn-content increases from MUS V-1 to V-3, resulting in a concentration of $MnO_2$ of 7 mol%, 13 mol%, and 17 mol% in the final products. The results are given in Table 2. A loss of about 5% of Li and 0–18% Mn occurred during the melting and cooling of the material. The MUS are therefore close in composition to the actual recycling slags studied by Elwert et al. [2].

**Table 2.** Comparison of the bulk chemical composition of the three melt experiments, given in mole percent.

| | **Raw Mix (Mole Fraction)** | | | **Product (Mole Fraction)** | | | **Recovery %** | | |
|---|---|---|---|---|---|---|---|---|---|
| | **V-1** | **V-2** | **V-3** | **V-1** | **V-2** | **V-3** | **V-1** | **V-2** | **V-3** |
| **$Al_2O_3$** | 32 | 29 | 28 | 33 | 31 | 29 | 103 | 107 | 104 |
| **CaO** | 16 | 14 | 14 | 15 | 15 | 14 | 94 | 107 | 100 |
| **$Li_2O$** | 21 | 19 | 18 | 20 | 18 | 17 | 95 | 95 | 94 |
| **MgO** | 3 | 3 | 3 | 3 | 3 | 3 | 100 | 100 | 100 |
| **$MnO_2$** | 7.4 | 13 | 17 | 6.1 | 12 | 17 | 82 | 92 | 100 |
| **$SiO_2$** | 22 | 21 | 20 | 23 | 22 | 21 | 105 | 105 | 105 |

### *4.2. Powder X-ray Diffraction*

The crystalline composition of the MUS V-1-3 was studied by PXRD and compared to an Mn-free material with comparable $LiAlO_2$-content. The compounds gehlenite, spinel and $LiAlO_2$ were present in all three slags (Figure 4a). The Li-Al-Oxide reflections are best explained with the diffraction pattern of $LiAlO_2$ (ICDD PDF2 no. 00-038-1464 [17]). A comparison of the reflection height of three mixtures with increasing Mn-concentration shows a negative correlation with the intensity of the $LiAlO_2$ main reflection. A comparison with an Mn-free material with comparable $Li_2O$ content (Figure 4c) indicates a strong negative influence of the Mn-concentration on the formation of $LiAlO_2$. The low intensities of the reflection and the comparable high background imply a high amount of amorphous material being present.

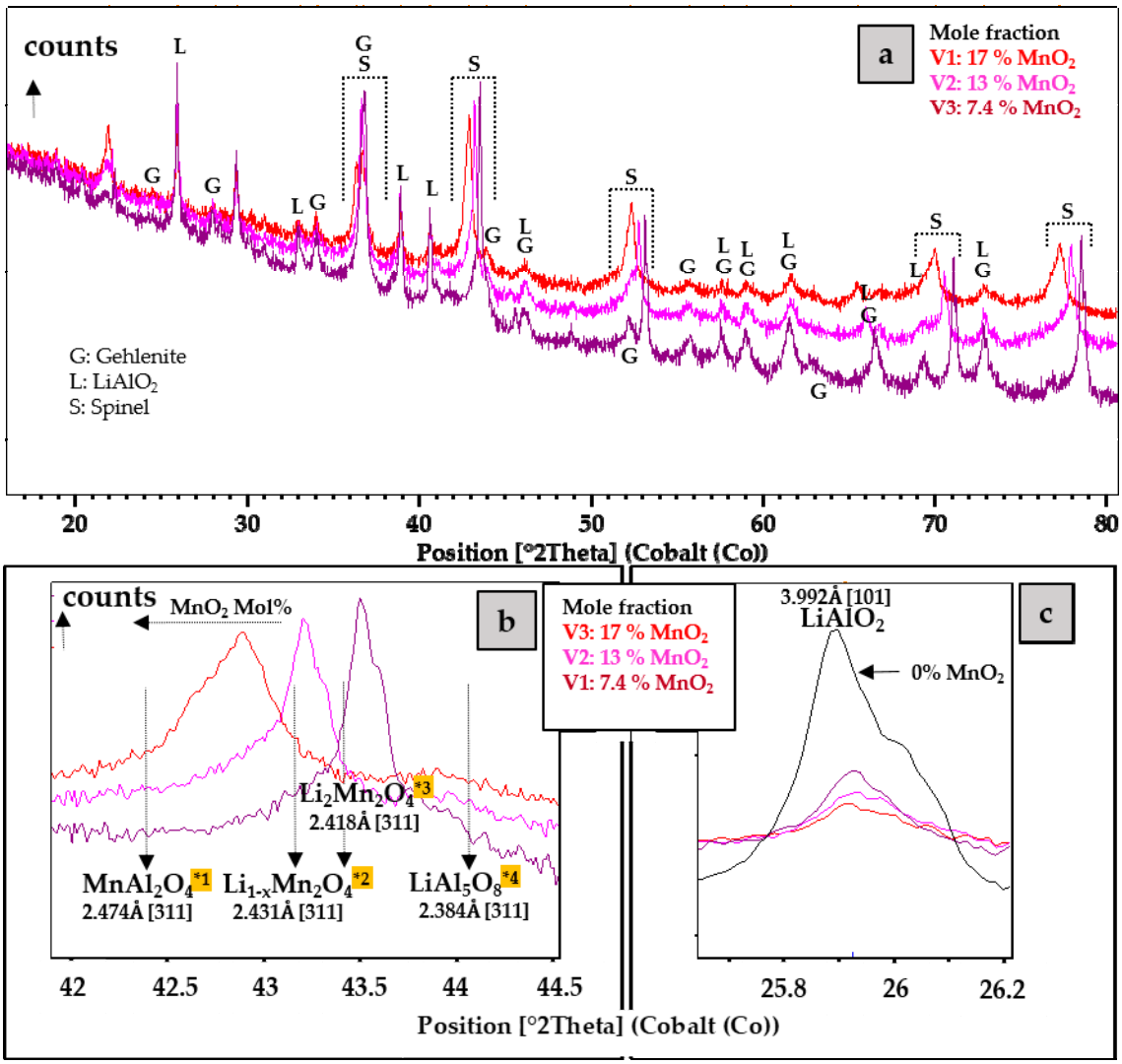


**Figure 4.** (**a**) Powder X-ray diffraction (PXRD) of the solidified melt. G: Gehlenite, S: Spinel, L: $LiAlO_2$. (**b**): Enlarged section of the main spinel peak. * 1: the position of the main peak of $MnAl_2O_4$ from the ICDD-PDF2 no. 00-029-0880 [17], * 2: the position of the main peak of the $Li_{(1-x)}Mn_2O_4$ spinel from the ICDD-PDF2 no. 00-038-07891 [17], * 3: the position of the main peak of the $Li_2Mn_2O_4$ spinel from the ICDD-PDF2 no. 01-084-1524 [17], * 4: the position of the main peak of the $LiAl_5O_8$ spinel from the ICDD-PDF2 no. 00-038-1425 [17], (**c**)**:** Enlarged sections of the first two main $LiAlO_2$ peaks. In (**c**): for comparison, the $LiAlO_2$ main reflection of an Mn-free solidified melt with comparable $Li_2O$ content is presented.

The enlarged section of the two-theta region of the main spinel reflections gives an indication of the changing composition of the spinel with the change of the Mn-content (Figure 4b). The main spinel reflections (311) of all three MUS lie between those of galaxite spinel $MnAl_2O_4$ and $LiAl_5O_8$. In this range, two reflections of Li/Mn-spinel are located ($Li_{1-x}Mn_2O_4$ and $Li_2Mn_2O_4$) [17]. This indicates the presence of a complex solid solution of a spinel-like oxide with the general formula $(Li_{(2x)}Mn^{2+}{}_{(1-x)})_{1+x}(Al_{(2-z)},Mn^{3+}{}_z)O_4$, which was derived by EPMA, as discussed below.

In conclusion, the PXRD results show the decrease of crystalline $LiAlO_2$ content with an increasing Mn-concentration. They also indicate the presence of a Li/Al/Mn spinel-like solid solution. The findings are consistent with the results of the microscopic EPMA analysis, which are presented in the following section.

### *4.3. Electron Probe Microanalysis*

The MUS with the highest $MnO_2$-content (MUS V-3, 17 mol%) was subjected to EPMA. From the PXRD results, it was expected that the microstructure of this sample would be most conclusive on the processes, resulting in a $LiAlO_2$-depleted material. The main compounds of the melt experiment V-3, determined with EPMA, were: a spinel phase $(Li_{(2x)}Mn^{2+}{}_{(1-x)})_{1+x}(Al_{(2-z)},Mn^{3+}{}_z)O_4$; lithium aluminate (LiAl) with the stoichiometric formula $Li_{1-x}(Al_{(1-x)}Si_x)O_2$; a gehlenite-like calcium-alumosilicate (GCAS) with the stoichiometric formula $Ca_2Al_2SiO_7$ and with minute amounts of Mg and Na (max. ~0.2 wt.%); and amorphous phases (APh) with various amounts of Al, Si, Ca, Mn, small amounts of Na (<0.3 wt.%), and sometimes with unusual elements like Ba and K (contaminants enriched in the eutectic residual melt).

The LiAl and the GCAS have already been described by Schirmer et al. [6] in a MUS not containing Mn but Li, Ca, Si, Al and Mg. There is strong evidence that the presence of Mn in the slag has an influence on the formation of Li and Al compounds. In particular, the formation of spinel solid solutions suggested by the PXRD is expected to influence the formation of $LiAlO_2$. Accordingly, the EPMA focused on elucidating the genesis of the Mn-rich grains. Overall, it was found that besides negligible amounts in amorphous phases, the Mn is almost exclusively incorporated into pure oxide (spinel) structures. For this reason, a detailed examination of a representative grain of Mn-containing oxide is presented in the following. Early crystallites of this type are predominantly found throughout the whole sample.

The BSE(Z) micrograph (Figure 5) shows a large grain of predominantly idiomorphic Mn-enriched oxide (spinel) surrounded by idiomorphic/hypidiomorphic grains of LiAl in a matrix of GCAS and accompanied by a grain of an APh enriched in unusual elements (contaminants), e.g., Ti and K probably representing the last eutectic melt composition.

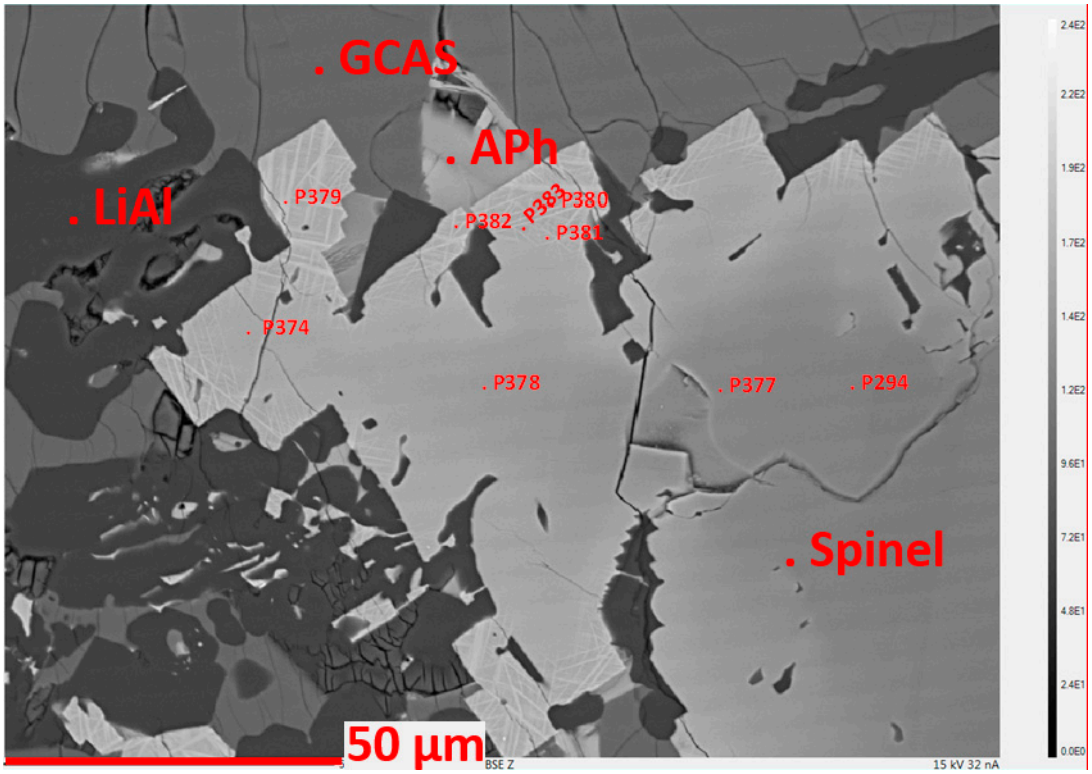


**Figure 5.** Electron micrograph (BSE(Z)) of the solidified melt. Light grey grain: spinel; dark gray sections, and dendrites: LiAl, surrounded by Ca-alumosilicate (GCAS, light grey sections); amorphous phases (APh): amorphous grain with unusual elements (K, Ba, Ti): contamination; black: pores or preparation damage. The chemical analysis of the points marked in red (P294–P383) is presented in Table 3.

**Table 3.** Elemental concentrations (wt.%) at the locations depicted in Figure 5, sorted in ascending order according to the Al concentration. For a close-up of the lamellae region, see Appendix C. The distance from the lamellae region points to the nearest rim is given. Regarding the point scans, a virtual line is drawn through all points to the left rim. The distances are given from each point to the intersection of this line with the rim.

| **Location** | **Lamellae Region** | | | | | **Point Scan** | | | |
|---|---|---|---|---|---|---|---|---|---|
| **No.** | **379** | **382** | **383** | **380** | **381** | **374** | **378** | **377** | **294** |
| **Distance from rim in µm** | 2.6 | 2.2 | 6.9 | 5.6 | 10.4 | 10.1 | 46.5 | 81.8 | 101.2 |
| **Al** | 0.7 | 0.7 | 1.5 | 1.5 | 3.1 | 6.0 | 11.9 | 16.7 | 22.3 |
| **Mg** | 0.1 | 0.1 | 0.1 | 0.1 | 0.1 | 0.1 | 0.2 | 0.2 | 0.5 |
| **Ti** | 0.4 | 0.4 | 0.3 | 0.2 | 0.1 | 0.0 | 0.0 | 0.0 | 0.0 |
| **Mn** | 69.7 | 64.4 | 62.9 | 64.0 | 62.2 | 60.0 | 52.3 | 46.9 | 39.0 |
| **Fe** | 0.3 | 0.4 | 0.5 | 0.5 | 0.5 | 0.4 | 0.3 | 0.3 | 0.3 |
| **Ca** | 0.2 | 0.1 | 0.1 | 0.2 | 0.1 | 0.2 | 0.0 | 0.0 | 0.0 |
| **Si** | 0.2 | 0.2 | 0.2 | 0.2 | 0.1 | 0.1 | 0.1 | 0.0 | 0.0 |

The gradient of the grey shade of the Mn-oxide grain indicates an increase of the mean atomic number from the center to the rim. At the outer edge, segregation lamellae can be observed. The brighter grey shade of these lamellae indicates a higher mean atomic number than in the surrounding grain. To investigate the changing composition from the inner part of the grain to the rim, several points were analyzed. Due to the relatively small features (<1–2 µm) of the segregation lamellae, the emphasis was on the precise determination of the whiskers. Therefore, the recording of a line scan was omitted. Table 3 contains the original data.

The concentrations found for Al and Mn were used to calculate normalized contents of Al and $Mn^{2+}$, $Mn^{3+}$ as well as the fractions of $LiMnO_2$, $Mn_{0.5}AlO_2$ (1/2 galaxite spinel), and $Mn_{0.5}MnO_2$ (1/2 hausmannite) fitting the three spinel components to the elemental amounts (Table 4). The Li-concentration was subsequently obtained from the calculated amount of $LiMnO_2$. The general formula obtained from the fittings is $(Li_{(2x)}{Mn^{2+}}_{(1-x)})_{1+x}(Al_{(2-z)},{Mn^{3+}}_z)O_4$. The minute concentrations of the other elements are omitted in this calculation. The results show that the Al content in the grain decreases during crystallization. The result of this calculation gives an indication that a solid solution of Li-Al-Mn spinel is formed.

**Table 4.** Spinel formulas, calculated with the Al and Mn concentrations of Table 3, sorted in ascending order according to the Al concentration. The $Mn^{2+}/Mn^{3+}$-ratio was calculated using the total measured Mn concentration in Table 3. The Li concentration is derived from the calculated fraction of $LiMnO_2$. In the first section of the table, the concentrations of the elements are given in weight percent. In the second section, the calculated fractions of the different virtual components in percent are presented. In the last section, the stoichiometric ratio of the formula $(Li_{(2x)}{Mn^{2+}}_{(1-x)})_{1+x}(Al_{(2-z)},{Mn^{3+}}_z)O_4$ is presented. The distance from the lamellae region points to the nearest rim is given. Regarding the point scans, a virtual line is drawn through all points to the left rim. The distances are given from each point to the intersection of this line with the rim.

| **Location** | **Lamellae Region** | | | | | **Point Scan** | | | |
|---|---|---|---|---|---|---|---|---|---|
| **No.** | **379** | **382** | **383** | **380** | **381** | **374** | **378** | **377** | **294** |
| **Distance from rim in µm** | 2.6 | 2.2 | 6.9 | 5.6 | 10.4 | 10.1 | 46.5 | 81.8 | 101.2 |
| Concentrations (wt.%) | | | | | | | | | |
| **Al** | 0.7 | 0.7 | 1.5 | 1.5 | 3.1 | 6.0 | 11.9 | 16.7 | 22.3 |
| **$Mn^{2+}$** | 21.5 | 12.2 | 11.5 | 13.6 | 14.5 | 17.9 | 19.3 | 21.8 | 22.7 |
| **$Mn^{3+}$** | 48.2 | 52.2 | 51.4 | 50.4 | 47.7 | 42.1 | 33.0 | 25.1 | 16.7 |
| **Li** | 0.8 | 3.7 | 4.0 | 3.3 | 3.2 | 2.4 | 2.4 | 2.0 | 2.1 |
| Calculated fractions (%) | | | | | | | | | |
| **$Mn_{0.5}AlO_2$** | 2.1 | 2.2 | 4.7 | 4.9 | 10.0 | 19.2 | 38.2 | 53.5 | 71.5 |
| **$LiMnO_2$** | 11.0 | 49.9 | 53.6 | 45.1 | 42.7 | 31.8 | 31.9 | 26.7 | 28.5 |
| **$Mn_{0.5}MnO_2$** | 86.9 | 47.9 | 41.7 | 50.0 | 47.3 | 48.9 | 29.9 | 19.9 | 0.0 |
| Stoichiometric factors $(Li_{2x}{Mn^{2+}}_{(1-x)})_{(1+x)}(Al_{(2-z)},{Mn^{3+}}_z)O_4$ | | | | | | | | | |
| $x$ | 0.13 | 0.54 | 0.58 | 0.49 | 0.46 | 0.34 | 0.33 | 0.26 | 0.27 |
| $z$ | 1.95 | 1.95 | 1.89 | 1.88 | 1.76 | 1.55 | 1.15 | 0.85 | 0.54 |

### *4.4. X-ray Absorption near Edge Structure*

To verify the structures suggested from EPMA analysis, XANES was conducted on the sample MUS V-3. For comparison, the spectra of known Mn oxidation states were recorded as well. In Figure 6, Mn K-edge XANES spectra of compounds representing oxidation states from $Mn^{2+}$ to $Mn^{4+}$ are displayed for comparison with the spectrum of the MUS.

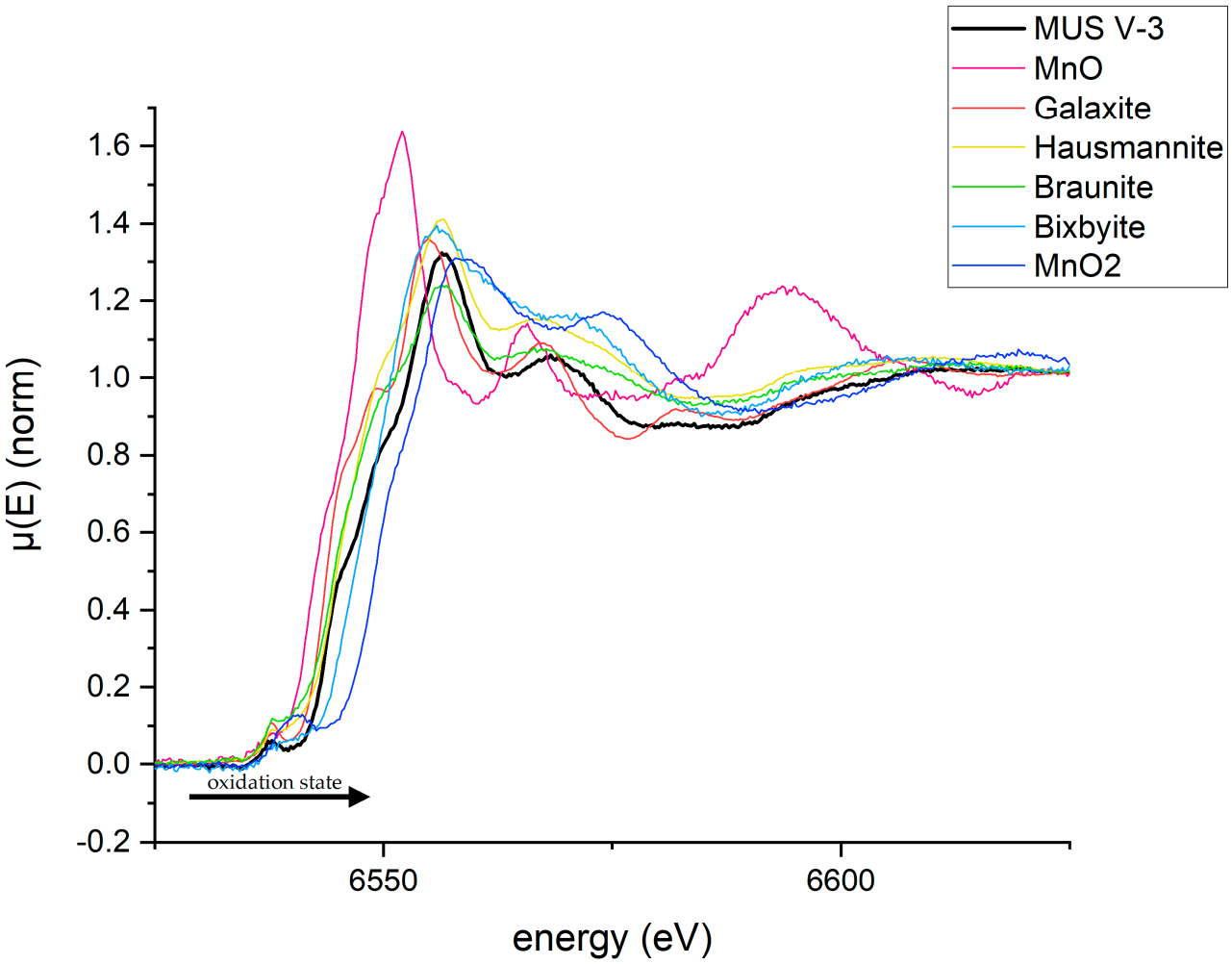


**Figure 6.** Spectra of Mn samples of different oxidation states. The spectra are compared to the spectrum of the mock-up slag (MUS). A shift of the edge accompanies the increase in the oxidation state which is indicated by the arrow. The mean oxidation states of Mn in the compounds are as follows: MnO: +2; galaxite: +2, hausmannite: +2.67; braunite: +2.85; bixbyite: +3; and $MnO_2$: +4.

A shift of the edge to higher energies with increasing oxidation state is observed (Figure 6); this is a well-known effect [27]. From the edge shift and the shape of the curve, it can be concluded that the oxidation state of Mn in the MUS is a mixture of +2 and +3. A mixture of +4 and +2 is unlikely. A combination of both would result in a relatively flat curve, which is not observed in the MUS spectrum. For a better overview of the correlation with oxidation states ranging from +2 to +3, see Appendix B.

According to the results of the Mn K-edge XANES of the reference samples, the average oxidation state of Mn has to be between +2 and +3. Additionally, the analysis via EPMA and PXRD strongly supports the presence of spinel structures involving Mn und Al. The XANES spectra show that Mn is not present in the pure form of any of the analyzed oxides. The same is concluded from the EPMA, which in addition has shown that the Al-percentage in these Mn phases is lower than in pure galaxite.

Accordingly, linear combinations of the spinels galaxite and hausmannite, as well as of galaxite and bixbyite, were calculated. From these linear combinations, the model XANES spectra in Figures 7 and 8 were obtained. These mixtures present a lower Al-content than galaxite, but still have a spinel structure. The results obtained from these linear combinations can be seen in Figures 7 and 8. A linear combination of hausmannite with bixbyite was also calculated. These results are shown in Appendix D.

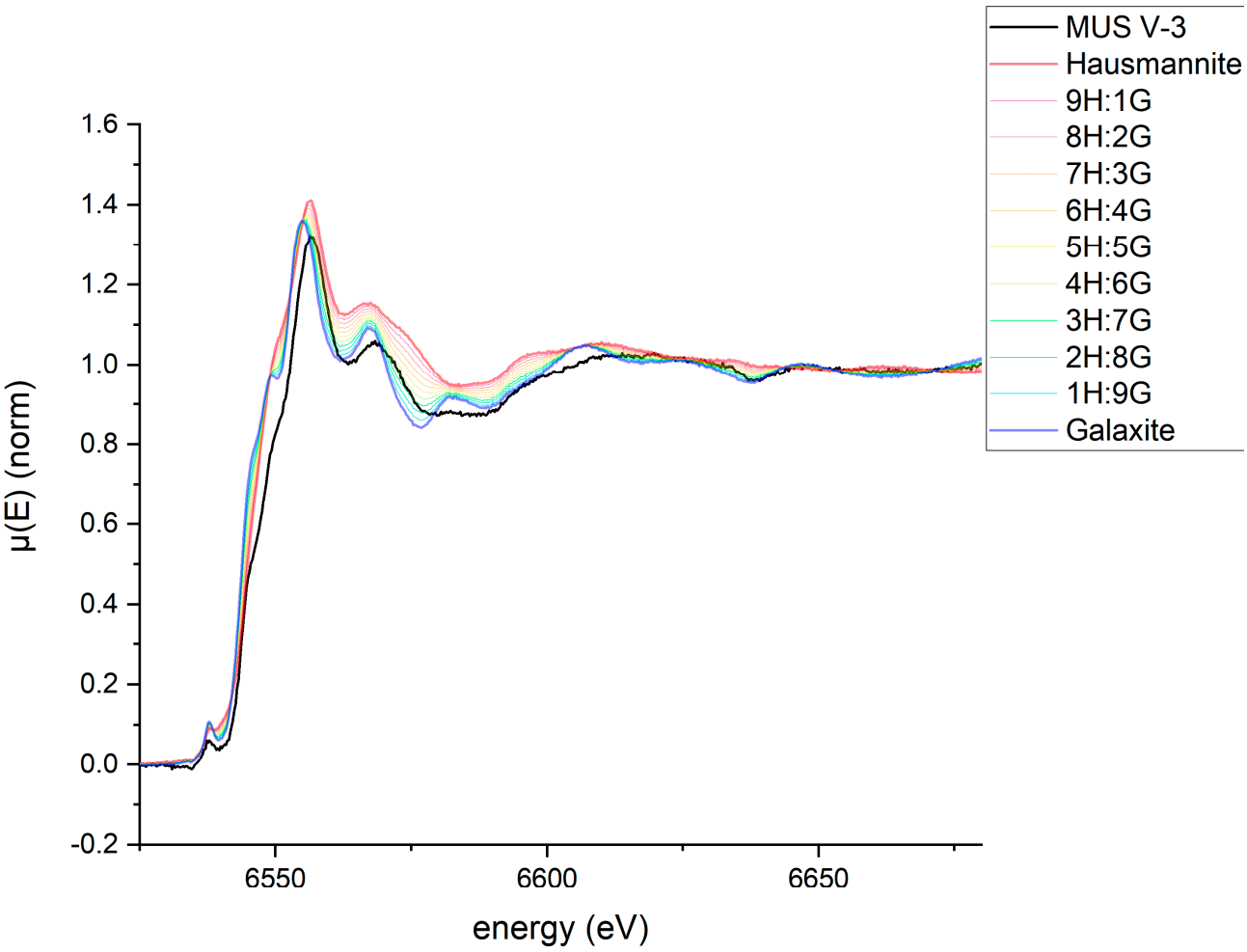


**Figure 7.** Linear combination of hausmannite (H) and galaxite (G). At the edge jump, the MUS spectrum fits the spectrum of hausmannite, whereas after the jump, the spectrum is more similar to galaxite.

The linear combinations (Figures 7 and 8) of a 50:50 (mass) mixture of both galaxite and bixbyite, as well as galaxite and hausmannite, are quite similar to the measured spectrum of the MUS V-3. A combination of bixbyite and hausmannite is excluded from further investigation, as the shape is significantly different (see Appendix D). Accordingly, the experimental XANES data was obtained from a 50:50 (mass) mixture of galaxite and bixbyite, as well as galaxite and hausmannite. The obtained spectra are shown in Figures 9 and 10. Figure 10 shows a close-up of the edge-jump.

The spectra displayed in Figures 9 and 10 show that the pre-edge, the edge jump and the region after the edge of the MUS and both references are similar. The results suggest that the slag contains a mixture of $Mn^{2+}$ and $Mn^{3+}$, confirming the EPMA analysis. The combinations of galaxite and bixbyite with an average Mn oxidation state of 2.69—as well as of galaxite and hausmannite, with an average oxidation state of 2.46—mostly match the MUS spectrum. In conclusion, galaxite is present in the MUS.

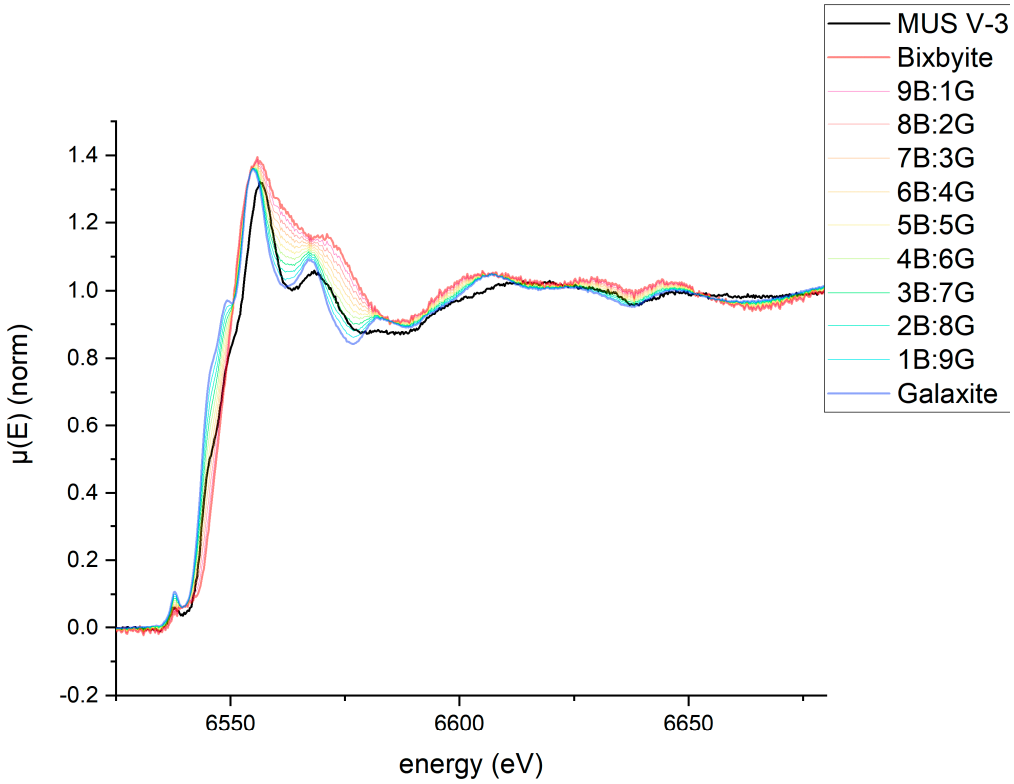


**Figure 8.** Linear combination of bixbyite (B) and galaxite (G). The spectrum of the MUS is similar to the linear combination. At the edge jump, the MUS spectrum fits the middle of the linear combination, whereas in the region after the edge, the spectrum is more similar to that of galaxite.

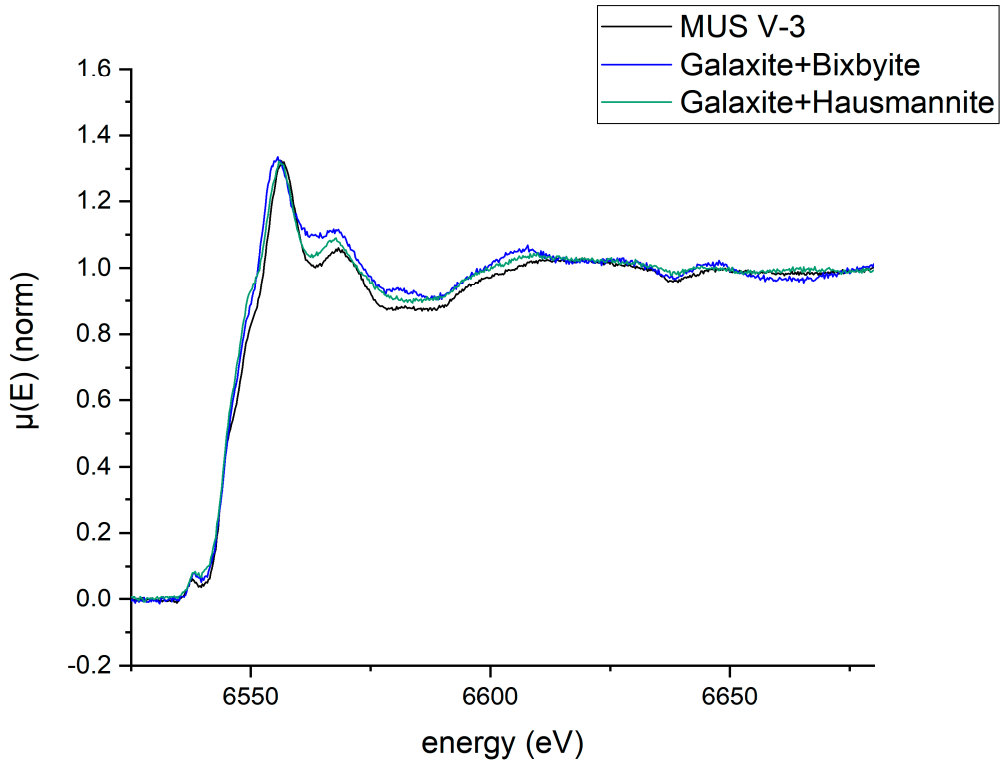


**Figure 9.** Experimentally derived X-ray absorption near edge structure analysis (XANES) spectra of a 50 wt.% mixture of galaxite and bixbyite, respective of galaxite and hausmannite compared to the spectrum obtained from the MUS V-3. The pre-edge peak, edge jump and course of the spectrum are very similar for all three spectra.

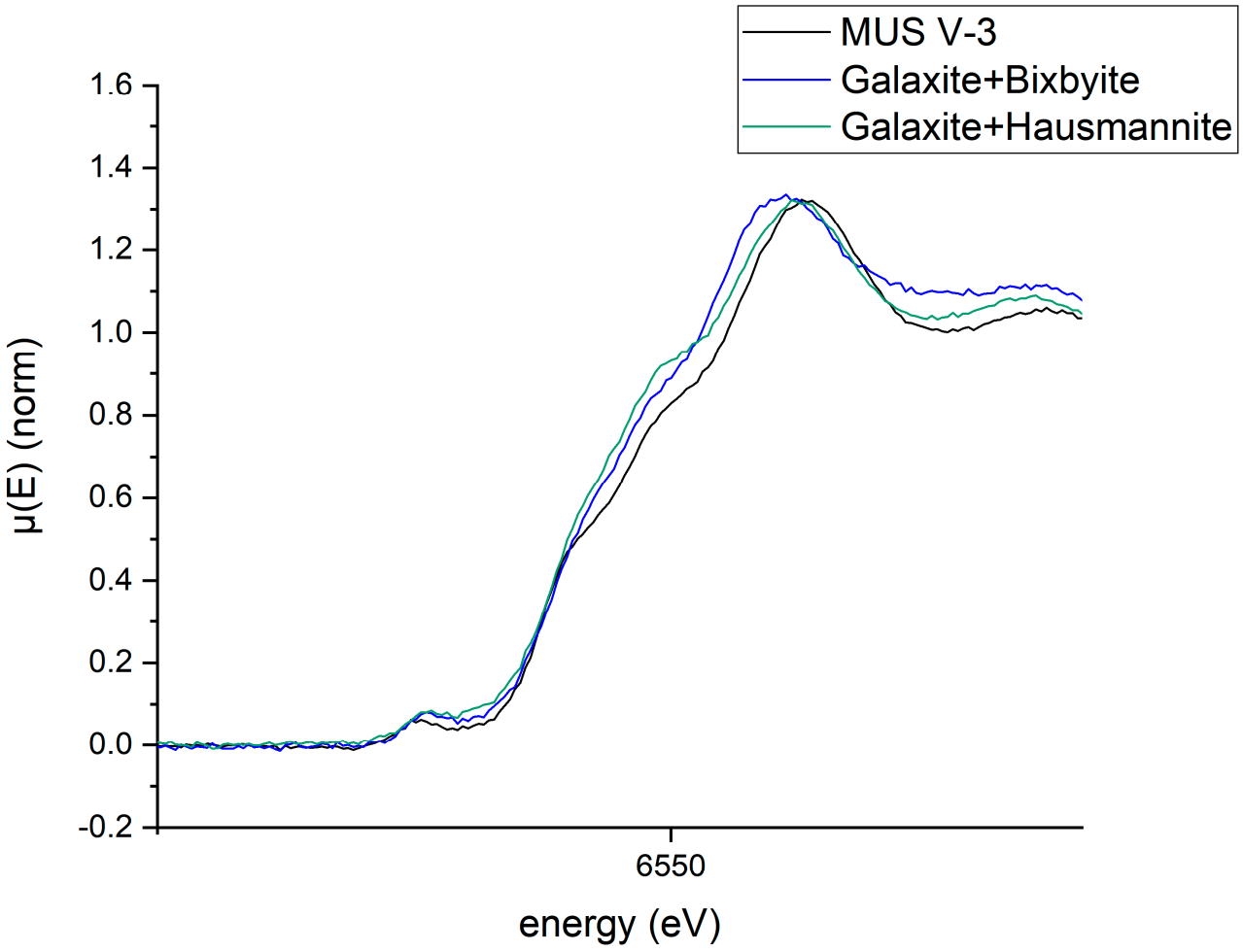


**Figure 10.** Close-up to the edge jump from Figure 9.

## 5. Discussion

The experimental investigation of the influence of Mn on the solidification, and especially on the formation of the EnAM $LiAlO_2$ in slags of the six-component oxide system (Li, Mg, Al, Si, Ca and Mn) is crucial to understand. This is also indispensable for the phase relations, as well as the reactions in this complex system. It will also help to predict the slag composition and improve thermodynamic modeling. Slags, unlike most geological features, are formed on a short timescale and with high cooling rates. Hence, non-equilibrium thermodynamic modeling will have to be consulted to develop a route to create the desired EnAM.

In contrast to the other elements in this system, Mn is redox-sensitive, occurring in several oxidation states ranging from +2 to +7. Due to the moderate to high oxygen fugacity in the slag, the expected oxidation numbers are +2, +3 and +4, and mixtures thereof. The purpose of this research was to study the suppression of $LiAlO_2$ formation in Mn-rich Li-ion battery recycling slags. The determination of the Mn-species, including the oxidation state formed in slags, is key to understanding this phenomenon.

Investigations with PXRD and EPMA on Mn-rich MUS reveal that besides LiAl and GCAS, the melt contains large grains of Al/Mn-rich oxides. The PXRD results show that these oxides can be best described as spinel-like compounds. The diffractograms exhibit reflections in the range of the main (311) diffraction line of the spinel-structures $MnAl_2O_4$ (galaxite), $Li_{1-x}Mn_2O_4$, $Li_2Mn_2O_4$ and $LiAl_5O_8$ (Figure 4). Due to the non-direct matching of these diffraction lines, the best explanation is a spinel solid solution with the elements Li, Al and Mn. With increasing Mn concentration within the melt experiments MUS V-1 to

V-3, there is a shift of the diffraction reflection towards galaxite, indicating that the galaxite component is increasing.

The amount of $LiAlO_2$ seems to be suppressed compared to an Mn-free melt with similar Li-concentration (Figure 4c, black line). Due to the high peak to background ratio, a comparable high amount of amorphous phase can be assumed.

The BSE(Z) micrograph observations show large idiomorphous Mn-rich grains (example see: Figure 5), suggesting an early and complex crystallization scenario. EPMA point scan analyses (Table 3) show a distinct decrease in the aluminum concentration from the center to the rim of the predominant Mn-rich crystals. At the edge, the aluminum concentration drops nearly to zero. Additionally, there is a split into two components, one relatively Mn-enriched and one relatively Mn-depleted. If the composition of all measurements is calculated as fractions of the virtual compounds $Mn_{0.5}AlO_2$ ($\frac{1}{2}$ galaxite), $LiMnO_2$ and $Mn_{0.5}MnO_2$ ($\frac{1}{2}$ hausmannite) a general formula $(Li_{(2x)}Mn^{2+}{}_{(1-x)})_{1+x}(Al_{(2-z)},Mn^{3+}{}_z)O_4$ can be calculated. From this calculation, a Li-content is derived and used to assess a gradient of the Li-bearing compounds. In accordance with the elemental gradients, a constant decrease of the galaxite fraction from the center to the rim is observed. In contrast, the hausmannite fraction is increasing. The Li-Mn compound fraction stays more or less constant except for a steep increase at the last ~10 µm from the rim. Directly at the rim, a split into a "normal" and a $Mn_{0.5}MnO_2$-dominated region can be observed. The increase and decrease of the individual species over the point scans are shown in Figure 11.

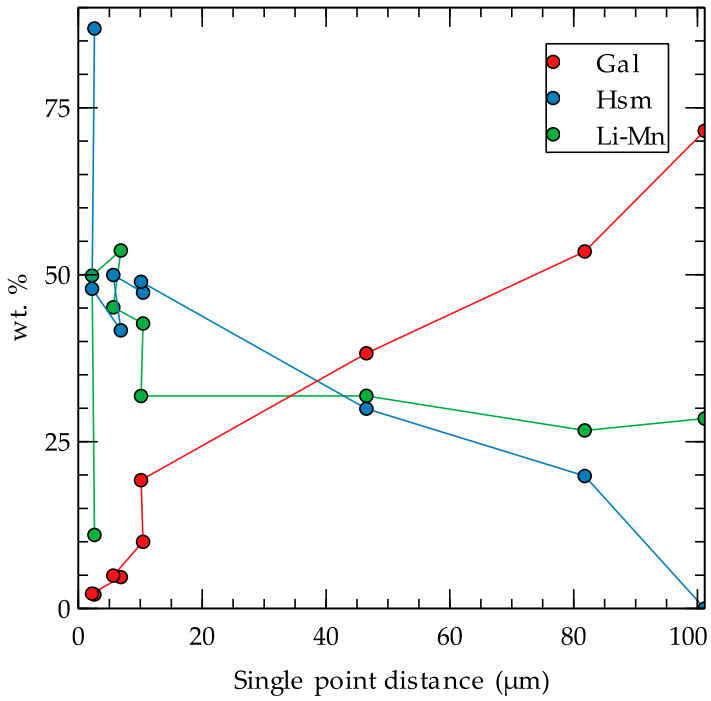


**Figure 11.** Fractions of the virtual compounds $Mn_{0.5}AlO_2$ ($\frac{1}{2}$ galaxite, Gal), $LiMnO_2$ (Li-Mn), and $Mn_{0.5}MnO_2$ ($\frac{1}{2}$ hausmannite, Hsm) in the grain presented in Figure 5.

This observation indicates that from the beginning to the end of the crystallization, Li is incorporated into the spinel structure. The spinel composition itself changes from a galaxite-dominated to hausmannite-dominated chemistry. Directly at the rim, the oversaturation of the melt with Mn is such that the spinel solid solution segregates (most probably during cooling down to room temperature) to form two different (most probably spinel-like) oxides.

In this respect, it is interesting that at lower temperatures, the hausmannite converts to the tetragonal crystal system with low solubility of the spinel compound galaxite as reported by Chatterjee et al. [9]. This could indicate an exsolution of the hausmannite

component due to crystal lattice incompatibility. The hypothesis is backed by the results from the Mn K-edge analysis, which suggests a mixture of galaxite and $Mn^{2+}$, $Mn^{3+}$ oxide spinels. The virtual Li compound would mix into the cubic galaxite-like spinel phase.

By combining the above results, a scenario of the large crystal genesis is established. The crystallization starts with a high aluminum galaxite-like composition that is subsequently enriched in Mn during the crystal growth. At the end of the crystallization, the solid solution becomes unstable, indicated by exsolution whiskers with a higher mean atomic number, surrounded by the massive crystal.

## 6. Conclusions

In this study, Mn-rich grains in mock-up slags (system: $Li_2O$-CaO-$SiO_2$-$Al_2O_3$-MgO-$MnO_x$) were characterized to understand the suppression of the $LiAlO_2$ formation in Mn-rich Li-ion battery recycling slags. The PXRD, EPMA and XANES data suggest that Mn-rich grains crystallize early on as a spinel solid solution. A generic stoichiometry, i.e., $(Li_{(2x)}Mn^{2+}{}_{(1-x)})_{1+x}(Al_{(2-z)},Mn^{3+}{}_z)O_4$ of the solid solution was determined assuming a combination of the virtual components $Mn_{0.5}AlO_2$, $LiMnO_2$ and $Mn_{0.5}MnO_2$. From the spatially resolved data, it was concluded that the solid solution is relatively Al-rich at the beginning of the crystallization and becomes depleted during the process. The formation of spinel solid solution with Mn and Al seems to scavenge Li from the melt before the $LiAlO_2$ crystallization can begin.

In conclusion, the experimental evaluation of mock-up slags has provided valuable insights into the Li, Mg, Al, Si, Ca, Mn and O system, and emphasized the benefit to study model melts and slags. In the future, however, an approach allowing for a faster synthesis of variable composition would be desirable. This approach will help to design suitable EnAM. The extraction of the EnAM from the slag and further processing will be part of subsequent studies.

In addition, it is not clear how these early crystals form on a molecular level. The solid solution could be a product of a solid phase process. It could also be driven by the ion-pair formation in the melt. In this respect, it is crucial to evaluate the primary crystallization fields in the system $Li_2O$-$Al_2O_3$-$MnO_x$ in the presence of the other slag compounds Mg, Si and Ca. Despite this, the influence of the viscosity and the oxygen concentration on the early formation of Mn-rich compounds needs to be studied. The impact of viscosity changes, and pair formation in the ionic melt could be accessed by molecular dynamic modeling.

**Author Contributions:** A.W. conceived the paper. A.W., U.E.A.F. and T.S. conducted the literature review. All melting experiments were designed and performed by H.Q. and D.G. The chemical bulk analysis was executed by the analysis laboratory of the Institute of Mineral and Waste Processing. The phase analysis (PXRD) and the mineralogical investigation (EPMA) were conducted by T.S. The speciation analysis with XANES and interpretation of the spectra was conducted by A.W. and U.E.A.F. Interpretation, discussion and conceptualization were conducted by all authors. All authors have read and agreed to the published version of the manuscript.

**Funding:** This research was funded by the Clausthal University of Technology in the course of a joint research project, "Engineering and Processing of Artificial Minerals for an Advanced Circular Economy Approach for Finely Dispersed Critical Elements" (EnAM).

**Acknowledgments:** We acknowledge support by Open Access Publishing Fund of Clausthal University of Technology. We thank Jörg Wittrock from the Institute of Inorganic and Analytical Chemistry for the idea and implementation of the galaxite synthesis. We thank Joanna Kolny-Olesiak for discussions and proofreading.

**Conflicts of Interest:** The authors declare no conflict of interest. The funders had no role in the design of the study, in the collection, analyses, or interpretation of data, in the writing of the manuscript, or in the decision to publish the results.

## Appendix A

The conversion from $\theta$-angle to energy space is done by following Bragg's law, with the order of diffraction ($n$), Planck constant ($h$), speed of light ($c$), interplanar distance ($d$).

$$E = \frac{n \cdot h \cdot c}{2 \cdot d \cdot \sin(\theta)} \tag{A1}$$

For a cubic system, $d$ is defined as: $d = \frac{a_0}{\sqrt{h^2 + k^2 + l^2}}$, with lattice spacing ($a_0$) and Miller indices ($h$, $k$, $l$). Therefore, the term $\frac{n \cdot h \cdot c}{2d}$ is dependent on the chosen crystal and the order of diffraction.

## Appendix B

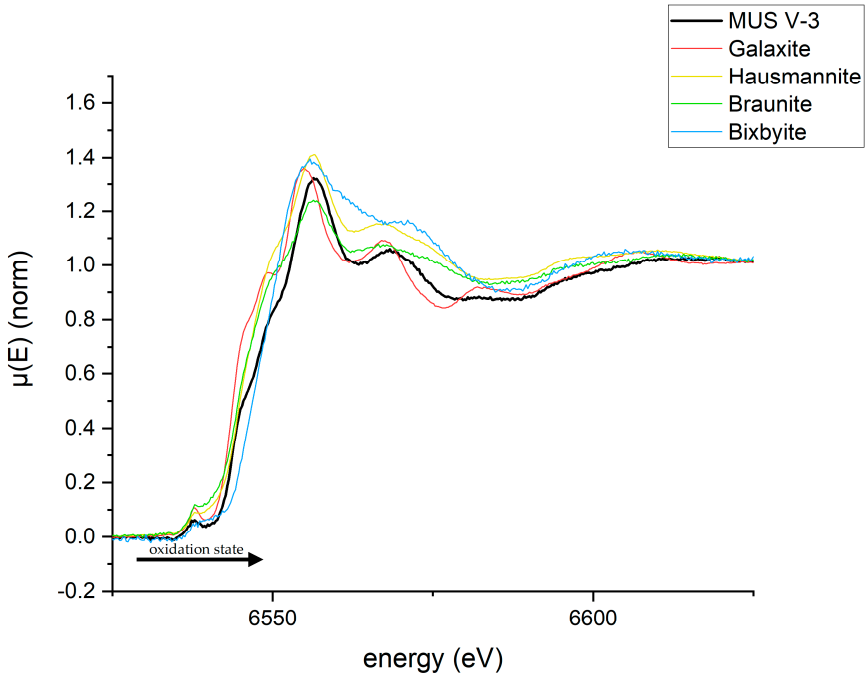


**Figure A1.** Spectra of Mn samples of different oxidation states. The spectra are compared to the measurement of the MUS. Oxidation states ranging for a better overview in contrast to Figure 6 from +2 to +3.

## Appendix C

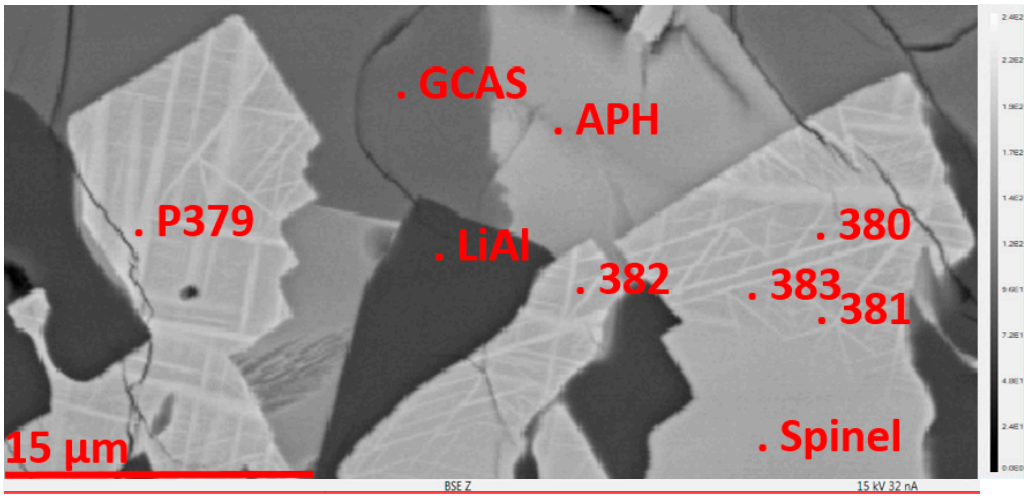


**Figure A2.** Close-up of Figure 4 showing the lamellae region.

## Appendix D

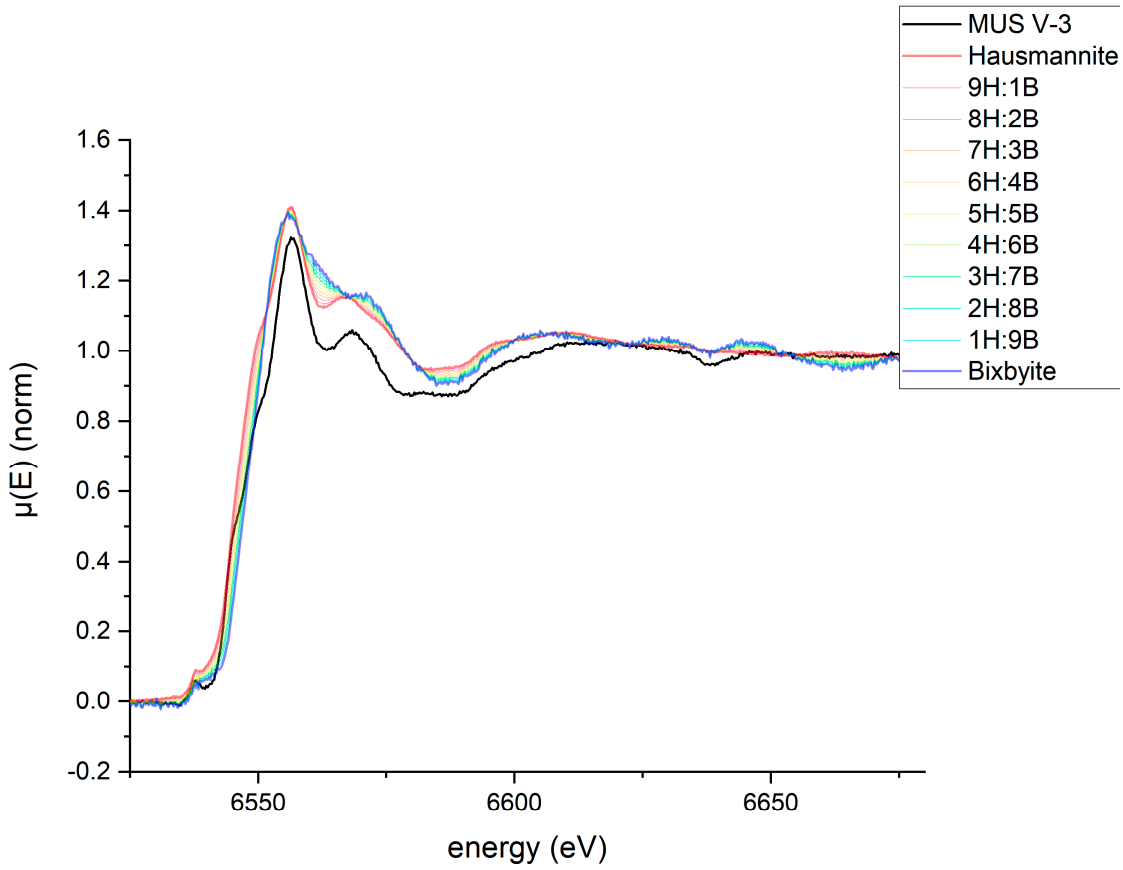


**Figure A3.** Linear combination of hausmannite (H) and bixbyite (B).

## References


1. Jaskula, B.W. Lithium. Available online: https://pubs.usgs.gov/periodicals/mcs2020/mcs2020-lithium.pdf (accessed on 15 December 2020).
2. Elwert, T.; Strauss, K.; Schirmer, T.; Goldmann, D. Phase composition of high lithium slags from the recycling of lithium ion batteries. *World Metall. -Erzmetall* **2012**, *65*, 163–171.
3. Velázquez-Martínez, O.; Valio, J.; Santasalo-Aarnio, A.; Reuter, M.; Serna-Guerrero, R. A Critical Review of Lithium-Ion Battery Recycling Processes from a Circular Economy Perspective. *Batteries* **2019**, *5*, 68. [CrossRef]
4. Haas, A.; Elwert, T.; Goldmann, D.; Schirmer, T. Challenges and research needs in flotation of synthetic metal phases: EMPRC 06/25-06/26/2018. In Proceedings of the European Mineral Processing & Recycling Congress, Essen, Germany, 25–26 June 2018; EMPRC, 2018. GDMB Verlag GmbH: Clausthal-Zellerfeld, Germany, 2018. ISBN 978-3-940276-84-1.
5. Elwert, T.; Goldmann, D.; Schirmer, T.; Strauss, K. *Recycling von Li-Ionen-Traktionsbatterien*; Recycling und Rohstoffe: Neuruppin, Germany, 2012; pp. 679–690.
6. Schirmer, T.; Qiu, H.; Li, H.; Goldmann, D.; Fischlschweiger, M. Li-Distribution in Compounds of the $Li_2O$-MgO-$Al_2O_3$-$SiO_2$-CaO System—A First Survey. *Metals* **2020**, *10*, 1633. [CrossRef]
7. Paulsen, J.M.; Dahn, J.R. Phase Diagram of Li–Mn–O Spinel in Air. *Chem. Mater.* **1999**, *11*, 3065–3079. [CrossRef]
8. Konar, B.; van Ende, M.-A.; Jung, I.-H. Critical Evaluation and Thermodynamic Optimization of the $Li_2O$-$Al_2O_3$ and $Li_2O$-MgO-$Al_2O_3$ Systems. *Met. Mater. Trans. B* **2018**, *49*, 2917–2944. [CrossRef]
9. Chatterjee, S.; Jung, I.-H. Critical evaluation and thermodynamic modeling of the Al–Mn–O (Al2O3–MnO–Mn2O3) system. *J. Eur. Ceram. Soc.* **2014**, *34*, 1611–1621. [CrossRef]
10. Asaoka, S.; Okamura, H.; Akita, Y.; Nakano, K.; Nakamoto, K.; Hino, K.; Saito, T.; Hayakawa, S.; Katayama, M.; Inada, Y. Regeneration of manganese oxide as adsorption sites for hydrogen sulfide on granulated coal ash. *Chem. Eng. J.* **2014**, *254*, 531–537. [CrossRef]
11. Kim, K.; Asaoka, S.; Yamamoto, T.; Hayakawa, S.; Takeda, K.; Katayama, M.; Onoue, T. Mechanisms of hydrogen sulfide removal with steel making slag. *Environ. Sci. Technol.* **2012**, *46*, 10169–10174. [CrossRef]

12. Seidler, G.T.; Mortensen, D.R.; Remesnik, A.J.; Pacold, J.I.; Ball, N.A.; Barry, N.; Styczinski, M.; Hoidn, O.R. A laboratory-based hard X-ray monochromator for high-resolution X-ray emission spectroscopy and X-ray absorption near edge structure measurements. *Rev. Sci. Instrum.* **2014**, *85*, 113906. [CrossRef]
13. Seidler, G.T.; Mortensen, D.R.; Ditter, A.S.; Ball, N.A.; Remesnik, A.J. A Modern Laboratory XAFS Cookbook. *J. Phys. Conf. Ser.* **2016**, *712*, 12015. [CrossRef]
14. Le, H.V.; Parishan, S.; Sagaltchik, A.; Göbel, C.; Schlesiger, C.; Malzer, W.; Trunschke, A.; Schomäcker, R.; Thomas, A. Solid-State Ion-Exchanged Cu/Mordenite Catalysts for the Direct Conversion of Methane to Methanol. *ACS Catal.* **2017**, *7*, 1403–1412. [CrossRef]
15. Dimitrakopoulou, M.; Huang, X.; Kröhnert, J.; Teschner, D.; Praetz, S.; Schlesiger, C.; Malzer, W.; Janke, C.; Schwab, E.; Rosowski, F.; et al. Insights into structure and dynamics of (Mn, Fe)Ox-promoted Rh nanoparticles. *Faraday Discuss.* **2018**, *208*, 207–225. [CrossRef]
16. Lutz, C.; Fittschen, U.E.A. Laboratory XANES to study vanadium species in vanadium redox flow batteries. *Powder Diffr.* **2020**, 1–5. [CrossRef]
17. Gates-Rector, S.; Blanton, T. The Powder Diffraction File: A quality materials characterization database. *Powder Diffr.* **2019**, *34*, 352–360. [CrossRef]
18. Downs, R.T.; Hall-Wallace, M. The American Mineralogist crystal structure database. *Am. Mineral.* **2003**, *88*, 247–250.
19. Lafuente, B.; Downs, R.T.; Yang, H.; Stone, N. The power of databases: The RRUFF project. In *Highlights in Mineralogical Crystallography*; Walter de Gruyter GmbH: Berlin, Germany, 2015; pp. 1–30. [CrossRef]
20. Jercinovic, M.J.; Williams, M.L.; Allaz, J.; Donovan, J.J. Trace analysis in EPMA. *IOP Conf. Ser. Mater. Sci. Eng.* **2012**, *32*, 12012. [CrossRef]
21. Merlet, C. Quantitative Electron Probe Microanalysis: New Accurate Φ (ρz) Description. *Mikrochim. Acta* **1992**, *12*, 107–115. [CrossRef]
22. Jahrman, E.P.; Holden, W.M.; Ditter, A.S.; Mortensen, D.R.; Seidler, G.T.; Fister, T.T.; Kozimor, S.A.; Piper, L.F.J.; Rana, J.; Hyatt, N.C.; et al. An improved laboratory-based X-ray absorption fine structure and X-ray emission spectrometer for analytical applications in materials chemistry research. *Rev. Sci. Instrum.* **2019**, *90*, 24106. [CrossRef]
23. easyXAFS, LLC. *easyXES100-Extended Executable Progra, Object Files, Documentation, and Source Code*; easyXAFS, LLC: Seattle, WA, USA, 2018.
24. Asakura, K.; Abe, H.; Kimura, M. The challenge of constructing an international XAFS database. *J. Synchrotron Radiat.* **2018**, *25*, 967–971. [CrossRef]
25. Itoh, T. K_MnO2_Si111_20110423. Available online: https://www.cat.hokudai.ac.jp/catdb/index.php?action=xafs_dbinpbrowsedetail&opnid=2&resid=22&r=32 (accessed on 30 November 2020).
26. Ravel, B.; Newville, M. ATHENA, ARTEMIS, HEPHAESTUS: Data analysis for X-ray absorption spectroscopy using IFEFFIT. *J. Synchrotron Radiat.* **2005**, *12*, 537–541. [CrossRef]
27. De Vries, A.H.; Hozoi, L.; Broer, R. Origin of the chemical shift in X-ray absorption near-edge spectroscopy at the MnK-edge in manganese oxide compounds. *Int. J. Quantum Chem.* **2003**, *91*, 57–61. [CrossRef]